Computers, Materials & Continua

Tech Science Press

https://doi.org/10.32604/cmc.2026.084636

ARTICLE

Interpretable AI for Non-Destructive Prediction of Electrode Properties from Frequency-Domain Ultrasonic Signals

Wasnaa Kadhim Jawad*

Businesses Informatics College, University of Information Technology and Communications, Baghdad, Iraq

*Corresponding Author: Wasnaa Kadhim Jawad. Email: wasnaakadhim@uoitc.edu.iq

Received: 04 May 2026; Accepted: 24 July 2026; Published: 15 September 2026

ABSTRACT: The accuracy of the electrode properties is important in the lithium-ion battery manufacturing process because the thickness variation is a direct influence on the compaction and structural uniformity, transport behavior and overall manufacturing quality. Of the different types of monitoring, ultrasonic frequency-domain relies on a non-destructive pathway for quality evaluation in a process-aware manner and is a promising approach; but, interpretable predictive modeling has been limited at the electrode level. In this study, an open-access database of ultrasonic frequency-domain data of lithium-ion battery electrodes under coating and calendering conditions was used to develop an artificial intelligence (AI) framework for predicting electrode thickness. The data set consisted of two subsets (anode and cathode) each of which included metadata, frequency bins and the associated magnitudes in a spectrum. It involved a combination of preprocessing, feature preparation, Stochastic Gradient Descent optimization of the Deep Neural Network (DNN) training process, and Shapley Additive Explanations (SHAP) for the post hoc analysis of the feature importances. To accommodate differences between the data sets, process variables, and spectral behavior, separate models were created for the anode and cathode sets. The results reported that the proposed framework has a good performance for the anode dataset, where the model got a mean absolute error of 9.530, root mean square error of 16.649, and coefficient of determination of 0.824. The values suggest that the model had a good predictive power on the relationship between ultrasonic frequency-domain input and electrode thickness. The interpretation stage also showed that the presence of certain components of the mid- and high-frequency spectra were important for the prediction of the anode, indicating a relationship between the acoustic response and the variations of material state caused by the manufacturing process. Furthermore, the overall dataset analysis revealed unique distribution in anode and cathode thickness, behavior under calendering state, and spectral-response patterns. The signals of the ultrasonic frequency domain can be effectively combined with deep learning and explainable AI to assist in interpretable thickness prediction, it was concluded. The proposed framework presents an excellent computational tool for non-destructive quality monitoring and intelligent manufacturing control in the production of advanced batteries.

KEYWORDS: Battery manufacturing; ultrasonic sensing; thickness prediction; explainable AI; deep neural network

1 Introduction

The rapid expansion of electrification technologies has intensified the need for advanced lithium-ion battery systems with high energy density, long cycle life, and stable electrochemical performance [1–3]. Achieving these requirements depends not only on electrode chemistry, but also on precise manufacturing control across the full production chain. In modern battery manufacturing, even small deviations in material distribution, porosity, coating uniformity, and structural compaction can propagate into significant variations in capacity retention, internal resistance, thermal behavior, and safety [4–6]. As a result, manufacturing

science has increasingly focused on data-related quality control, in-line sensors and smart monitoring to minimize waste, ensure product quality, and enable scale-up of large-scale production. In this respect, linking sensing, signal processing and machine learning has become an important avenue to enhance process transparency and improve our understanding of complex manufacturing processes.

Coating and calendering are crucial steps in the production of battery electrodes, as they define the thickness, density and microstructure of the resulting electrodes [7,8]. These factors influence the structure and pathways for ionic and electronic transport, mechanical stability, and ultimately battery performance, and must be well characterized to optimize the process [9,10]. Traditional offline measurements can be informative, but they are typically slow, destructive, and not suitable for real-time industrial applications. As such, non-destructive ultrasonic measurements have emerged as a potential tool for monitoring as they are sensitive to structural alterations and variations in the state of materials. When represented in the frequency domain, ultrasonic signals can reveal characteristic patterns associated with electrode condition and process-induced transformations, thereby offering a valuable basis for computational modeling, predictive analysis, and interpretable quality assessment in battery electrode manufacturing.

The study provides an overview in Table 1 of recent important works on monitoring battery manufacturing, ultrasonic property characterization, and quality assessment using machine learning, highlighting their limitations. As indicated, recent studies have demonstrated the following significant advances: ultrasonic sensing, transfer learning, digital manufacturing, virtual quality gates, and non-destructive defect applications. Yet, several limitations remain in the studies, including a lack of direct research focus on interpretable thickness prediction, the predominance of review articles, limited data validation at the battery-electrode scale using ultrasonic frequency-domain data, and inadequate incorporation of interpretability into predictive models. These shortcomings suggest that there remains a need for a more designed and explainable computational framework to evaluate battery electrode thickness.

Table 1: Summary of the most relevant recent studies on battery-manufacturing monitoring, ultrasonic characterization, and machine-learning-based quality analysis.

Ref.	Methodology	Main Finding	Limitation
[11]	Ultrasound + deep learning + cGAN	Accurate non-contact thickness prediction	Focused on thickness prediction, with limited emphasis on model interpretability; depends on a pilot-line dataset and deep architecture that may increase computational complexity
[12]	Frequency-domain ultrasonic dataset	Released a benchmark-ready open dataset	A data article rather than a predictive methodology paper; it does not itself develop a full interpretable predictive framework
[13]	Review of calendering models	Hybrid modeling is promising	Being a review, it does not present a direct predictive implementation; it also highlights that many existing models struggle to balance physical realism and industrial applicability
[14]	Review of inline ultrasonic monitoring	Ultrasound is promising	Focused on slurry mixing rather than final electrode thickness prediction

(Continued)

Table 1 (continued)

Ref.	Methodology	Main Finding	Limitation
[15]	Review of transfer learning	Transfer learning may help small-data cases	Does not provide a direct solution for ultrasonic electrode thickness prediction
[16]	ML-based virtual quality gates	Supports earlier quality decisions	Focused on assembly-line quality gates, not specifically on ultrasonic electrode characterization
[17]	Non-destructive defect detection	Defects can be detected during production	Focused on defect detection not thickness prediction; scope is more quality-screening oriented than interpretable AI modeling of manufacturing parameters
[18]	Review of AI-based optical inspection	AOI has strong potential in battery manufacturing	Concentrates on optical inspection, not ultrasonic sensing; review nature means no direct predictive framework or interpretability demonstration for thickness estimation
[19]	Review of AI-driven manufacturing frameworks	AI can improve battery manufacturing workflows	Broad systems-level discussion; lacks a specific experimentally framework for ultrasonic frequency-domain electrode thickness prediction with explainability
[20]	Physics-assisted DL–DEM model	Accurately predicts slurry-drying microstructure and reduces simulation time	Focused on simulated slurry drying rather than ultrasonic monitoring or electrode-thickness prediction

Despite the growing body of work on battery-manufacturing monitoring, important research gaps remain at the electrode level. While prior research has primarily focused on general quality, defect prediction, discussion, and highly specific deep learning tools, relatively few studies have explored explainable thickness prediction based on ultrasonic frequency features related to coating and calendering states. Specifically, the integration of ultrasonic frequency variables at the level of the electrode, process-related metadata, deep neural prediction, and post hoc explanation has not been sufficiently explored. This highlights the need for a computational approach that not only accurately predicts the electrode thickness, but also explains which spectral and process variables play a significant role in the prediction. The main contributions of this work are summarized as follows:

- A frequency-domain ultrasonic learning framework is established for non-destructive prediction of lithium-ion battery electrode thickness.
- Separate DNN-SGD models are developed for anode and cathode datasets to reflect electrode-specific signal behavior and process variables.
- SHAP interpretation is used to reveal the key spectral and manufacturing features influencing the predicted thickness.

The remainder of this manuscript is organized as follows. Section 2 presents the experimental work and describes the dataset source, structure, and main variables. Section 3 introduces the artificial intelligence approach, including the DNN-SGD prediction framework and the explainability stage. Section 4 provides the results and discussion, covering model performance, predictive behavior, and feature-importance interpretation. Finally, Section 5 concludes the manuscript and summarizes the main findings.

2 Experimental Dataset

The data set utilized in this work is taken from [12] which is an open-access ultrasonic frequency-domain data set covering the lithium-ion battery electrode coated and calendered specimen. The main features of the dataset used in this work from [12] are presented in Table 2. The data is currently presented in two separate sets: anode and cathode, with different numbers of samples, metadata, and FFT length, so it is assumed that they belong to two different sets, but are related. The data is stored in JSON format both as frequency domain signatures of ultrasound and as process cognition-aware metadata that enables the connection between the characteristics and features of the ultrasound signals and manufacturing knowledge. Such features allow the data to be used for data-driven thickness prediction and also enable a more insightful examination of potential differences between process conditions, ultrasonic response, and electrode types.

Table 2: Main specifications of the ultrasonic frequency-domain data used for battery electrode thickness analysis.

Item	Anode Dataset	Cathode Dataset
Sample range	GA_1 to GA_30	NMC622_1 to NMC622_18
Number of samples	30	18
States per sample	Before calendering, After calendering	Before calendering, After calendaring
Total records	60	36
File format	JSON	JSON
Signal representation	Frequency-domain ultrasonic data	Frequency-domain ultrasonic data
Main signal fields	fft_frequency, fft_magnitude	fft_frequency, fft_magnitude
Main metadata fields	Sample_ID, Calendering_Speed, Roll_Gap, Thickness, Density, Calendering_State	Sample_ID, Web_speed, Roll_Gap, Coat_Weight, Thickness, Density, Calendering_State
FFT length	36 frequency points	29 frequency points
Primary target used in this study	Thickness	Thickness

Fig. 1 presents a visual overview of the dataset structure, contents, and role in the present study. As shown, the dataset is composed of separate anode and cathode subsets, comprising 60 and 36 records, respectively, for a total of 96 usable records. Each sample state is stored in JSON format and contains three main components: metadata, fft_frequency, and fft_magnitude. The figure also highlights the main process-related and physical variables associated with the electrode manufacturing stages, including roll gap, speed

or web speed, coat weight, thickness, and density. In addition, it summarizes how the dataset was used in this study, where frequency-domain features were processed through the DNN-SGD framework and subsequently interpreted using SHAP-based analysis for thickness prediction.

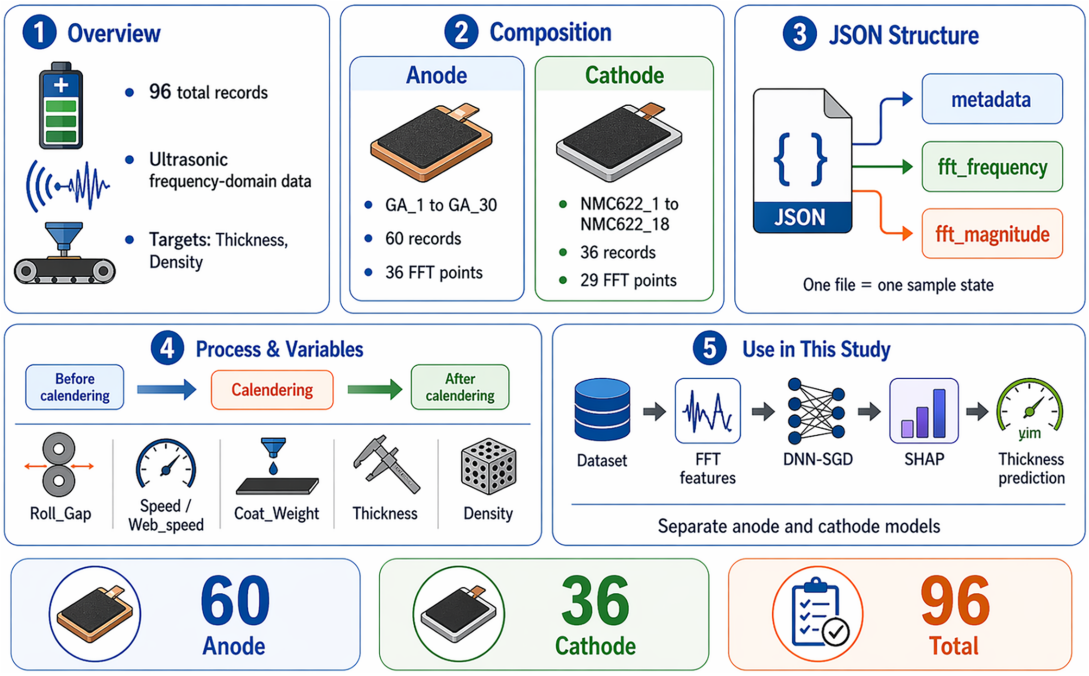

Figure 1: Overview of the ultrasonic frequency-domain dataset for lithium-ion battery electrodes.

3 Methodology

Section 3 presents the methodology adopted for the artificial intelligence stage of this work. It describes the preprocessing of the ultrasonic frequency-domain dataset, the feature preparation strategy, the development of the DNN-SGD model for thickness prediction, the validation procedure used for the anode and cathode subsets, and the SHAP-based interpretation approach applied to explain the contribution of the most influential input features.

3.1 Deep Neural Network (DNN)

Artificial intelligence has become widely used across diverse applications, including healthcare, finance, autonomous systems, manufacturing, image analysis, and predictive decision support, because of its ability to learn complex relationships from data and improve analytical performance [21–24]. Machine learning is part of this AI methodology in various fields of interest [25,26]. In materials-related fields, AI has been increasingly applied for property prediction, process optimization, defect detection, microstructure analysis, and intelligent quality monitoring [27–30]. DNNs can capture nonlinear high-dimensional patterns; their general forward propagation form is:

$$\mathbf{a}^{(l)} = f^{(l)}\left(\mathbf{W}^{(l)}\mathbf{a}^{(l-1)} + \mathbf{b}^{(l)}\right), l = 1, 2, \ldots, L \tag{1}$$

with

$$\hat{y} = \mathbf{a}^{(L)} \tag{2}$$

where:

- $\mathbf{a}^{(l-1)}$ is the input to layer l
- $\mathbf{W}^{(l)}$ is the weight matrix
- $\mathbf{b}^{(l)}$ is the bias vector
- $f^{(l)}(\cdot)$ is the activation function
- L is the number of layers
- $\hat{y}$ is the predicted output

This is the main structural equation for the DNN.

3.2 Stochastic Gradient Descent (SGD)

The standard SGD weight-update rule is [31]:

$$\theta_{t+1} = \theta_t - \eta \nabla_\theta \mathcal{L}(\theta_t; x_i, y_i) \tag{3}$$

where

- θ_t is the parameter vector at iteration? t
- η is the learning rate
- $\nabla_\theta \mathcal{L}(\theta_t; x_i, y_i)$ is the gradient of the loss for one sample or a mini-batch
- x_i and y_i are the input and target
- θ_{t+1} is the updated parameter vector

This is the main optimization equation for SGD.

3.3 Proposed DNN-SGD

For a DNN trained by SGD for regression, the combined loss-minimization form can be written as:

$$\min_\theta \mathcal{J}(\theta) = \frac{1}{N} \sum_{i=1}^{N} (y_i - f_\theta(x_i))^2 \tag{4}$$

and the parameters are updated by:

$$\theta_{t+1} = \theta_t - \eta \nabla_\theta \left[\frac{1}{m} \sum_{i=1}^{m} (y_i - f_\theta(x_i))^2 \right] \tag{5}$$

where:

- $f_\theta(x_i)$ is the DNN prediction for sample i
- y_i is the true target value
- N is the total number of samples
- m is the mini-batch size
- θ represents all weights and biases in the DNN
- η is the learning rate

Algorithm 1 summarizes the overall training and evaluation procedure of the proposed DNN-SGD framework for thickness prediction. As shown, the process was conducted separately for the anode and cathode datasets and involved cross-validation-based training, iterative weight updating through stochastic

gradient descent, early stopping based on validation behavior, performance assessment using MAE, RMSE, and R^2, and a final SHAP-based interpretation stage to determine the most influential input features.

Algorithm 1: Training procedure of the proposed DNN-SGD model for thickness prediction

for each dataset $D \in \{\text{Anode, Cathode}\}$ **do**
  for each cross-validation fold $k = 1, 2, \ldots, K$ **do**
    for each epoch $e = 1, 2, \ldots, E$ **do**
      for each mini-batch $B \subset D_{\text{train}}^{(k)}$ **do**
      perform forward propagation through the DNN to compute $\hat{y}$
      compute the loss using mean squared error
      perform backpropagation to obtain gradients of weights and biases
      update network parameters using SGD
        if validation loss does not improve for predefined iterations **then**
        stop training early
        end if
      end for
    end for
  evaluate the trained model on $D_{\text{test}}^{(k)}$ using MAE, RMSE, and R^2
  end for
aggregate the predictions from all folds and determine overall performance
apply SHAP analysis to identify the most influential input features
end for

With a relatively small dataset of only about one hundred instances, due to the high-dimensional and nonlinear nature of the ultrasonic frequency-domain features, regularization, early stopping, cross validation and comparisons with baseline (Other models) were used to minimize risk of overfitting and to objectively assess the value of the proposed model. The dataset specific preprocessing related to the dataset, the validation settings, the network architecture, the training-control parameters, and the optimizer configuration used in the proposed DNN-SGD framework are summarized in Table 3.

Table 3: Training and DNN-SGD hyperparameters used for thickness prediction in the anode/cathode datasets.

Category	Parameter	Anode Dataset	Cathode Dataset
Data/Target	Prediction target	Thickness	Thickness
	Dataset type	Anode ultrasonic frequency-domain data	Cathode ultrasonic frequency-domain data
	Input variables	Full FFT magnitudes + Density + Roll Gap	Full FFT magnitudes + Density + Roll Gap + Coat Weight
Validation	Cross-validation type	K-Fold cross-validation	K-Fold cross-validation
	Number of folds	5	3
	Shuffle	Yes	Yes
	Random state	42	42

(Continued)

Table 3 (continued)

Category	Parameter	Anode Dataset	Cathode Dataset
Preprocessing	Missing-value handling	Median imputation	Median imputation
	Input scaling	StandardScaler	StandardScaler
Model Architecture	Model type	DNN-SGD	DNN-SGD
	Hidden-layer structure	(32, 16)	(8)
Optimizer Setting	Activation function	ReLU	ReLU
	Solver/optimizer	SGD	SGD
	Learning-rate scheme	Adaptive	Adaptive
Training Control	Initial learning rate	0.0005	0.0005
	Momentum	0.80	0.70
	L2 regularization (alpha)	0.001	0.010
	Early stopping	Yes	Yes
	Validation fraction	0.20	0.20
	n_iter_no_change	35	35
	Maximum iterations	5000	5000
	Tolerance	1e−5	1e−5
	Random state	42	42

3.4 SHAP (Shapley Additive Explanations)

SHAP (Shapley Additive Explanations) has become a widely adopted explainable artificial intelligence technique for interpreting complex machine-learning models by quantifying the contribution of each input feature to the final prediction outcome. The SHAP explanation model is:

$$g\left(z'\right) = \phi_0 + \sum_{j=1}^{M} \phi_j z'_j \tag{6}$$

and the Shapley value for feature j is:

$$\phi_j = \sum_{S \subseteq F \setminus \{j\}} \frac{|S|!\left(M - |S| - 1\right)!}{M!} \left[f_{S\cup\{j\}}\left(x_{S\cup\{j\}}\right) - f_S\left(x_S\right) \right] \tag{7}$$

where:

- $g\left(z'\right)$ is the additive explanation model
- ϕ_0 is the base value
- ϕ_j is the contribution of feature j
- M is the total number of features
- S is a subset of features excluding feature j

- F is the full feature set
- $f_{S\cup\{j\}}\left(x_{S\cup\{j\}}\right)$ is the model output when feature j is included
- $f_S\left(x_S\right)$ is the model output without feature? j

The flow chart of the methodology used in this work for attribute interpretation of the battery electrode thickness is shown in Fig. 2. This workflow involves inputting the anode and cathode datasets, followed by the JSON data engine for data parsing, metadata, fft_frequency, and fft_magnitude extraction. The data are then separated, parsed, preprocessed, and used to train the DNN-SGD model. The network models are then assessed using MAE, RMSE, and R^2, followed by model interpretation using SHAP to determine the most significant features for the battery thickness prediction.

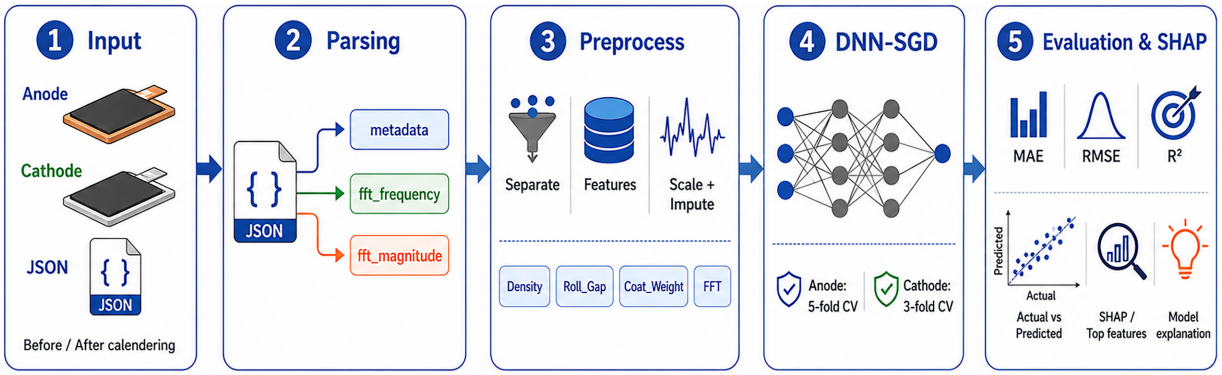

Figure 2: Workflow of data processing, thickness prediction, and SHAP-based interpretation.

4 Results and Discussion

This section presents the predictive results and their interpretation by examining the statistical behavior of the target variable and the performance of the DNN-SGD framework for the anode and cathode datasets.

4.1 Experimental Results Visualization

Fig. 3 illustrates the thickness distributions of both electrode datasets and provides an initial view of the variability that the prediction model must learn. As shown, the two subsets also have different spread and concentration patterns, supporting the idea that they are different modeling problems during both training and evaluation. As seen in Fig. 3a, the thickness of the anodes falls into a relatively wide range, from about 30 to 170, and there is a notable cluster around the middle range of 80–110. Additional observations can be distinguished in the gaps between 40 and 60, 110 and 130, and 140 and 160, indicating wider variation and a more spread-out target structure in the anode dataset. This wider spread indicates a more difficult regression space as the model needs to cover thickness behavior in low, medium, and high ranges as opposed to just around a central narrow band. Fig. 3b, on the other hand, shows that the thickness of the cathode is restricted to around 50–100, with the maximum thickness occurring around 88–90. The distribution of cathodes is narrower than the anode distribution, and there are recognizable values around 60–80, as well as a few at 95–100. The narrower cathode thickness distribution suggests stronger local prediction sensitivity, while Fig. 4 confirms that calendering reduces thickness in both electrode datasets.

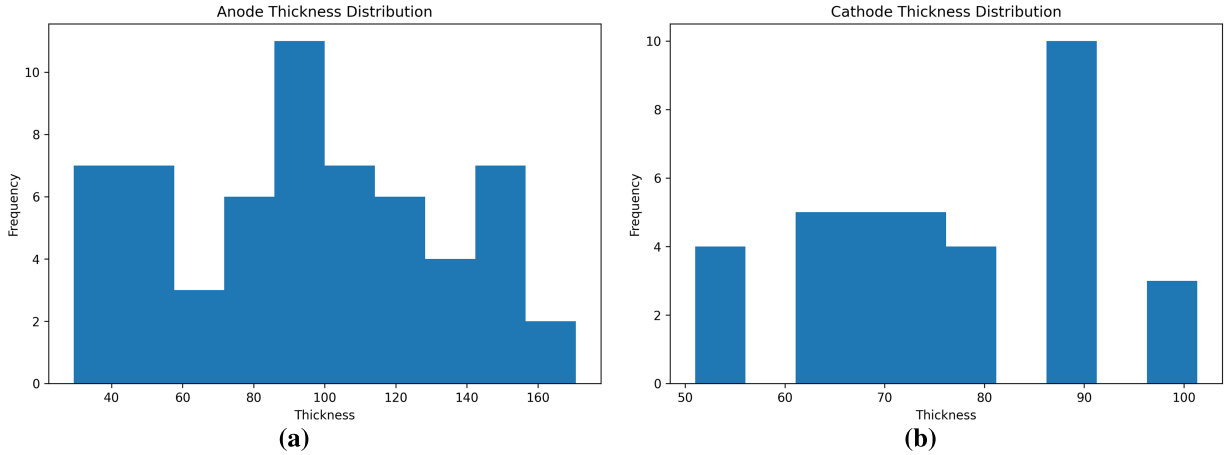

Figure 3: Thickness distribution of the battery electrode datasets used in this study: (**a**) anode thickness distribution; (**b**) cathode thickness distribution.

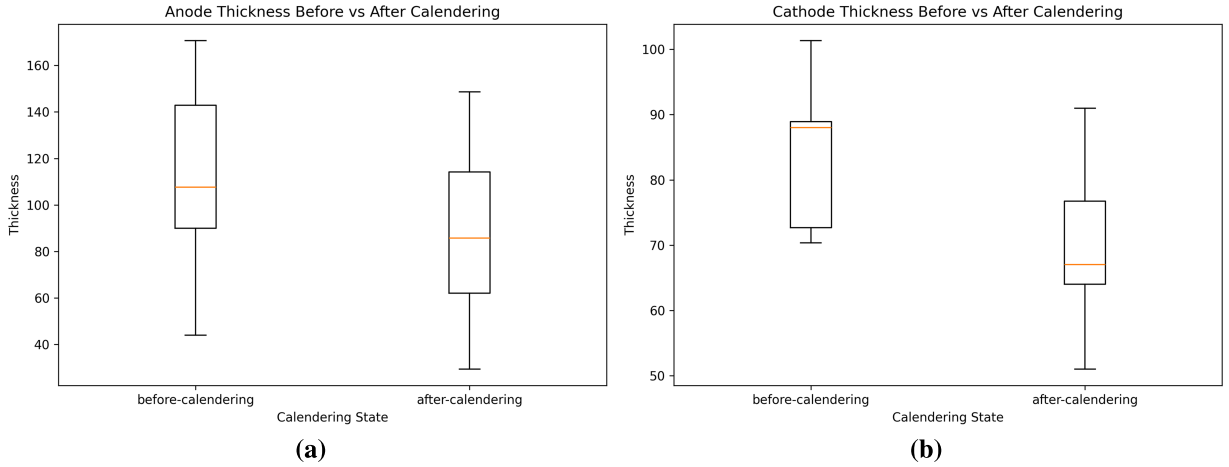

Figure 4: Comparison of electrode thickness before and after calendering for the studied datasets: (**a**) anode thickness before vs. after calendering; (**b**) cathode thickness before vs. after calendaring.

Fig. 5 presents representative frequency-domain ultrasonic spectra for the anode and cathode datasets before and after calendering, thereby illustrating how the spectral response changes with processing state. Overall, the figure shows that both electrode types exhibit their strongest responses in the lower-frequency region. At the same time, the post-calendering behavior differs in magnitude and decay pattern depending on the electrode type. Fig. 5a shows that the representative anode spectra contain multiple peaks and a broader frequency response than the cathode case. Before calendering, strong peaks can be observed near approximately 2.5 and 3.2, with normalized magnitudes approaching about 0.88 and 1.00, respectively, while after calendering the dominant peak remains close to 3.2 with a magnitude of about 1.00 and an additional elevated response appears around 4.8–5.8, where the magnitude remains between 0.45 and 0.63. In the higher-frequency range, the pre-calendering signal still preserves noticeable amplitudes around 8–9, reaching nearly 0.30–0.32, whereas the post-calendering signal decays more gradually after about 6 and becomes very small beyond approximately 10–11. This behavior suggests that calendering modifies the dominant peak intensity distribution and the anode's mid-frequency spectral content.

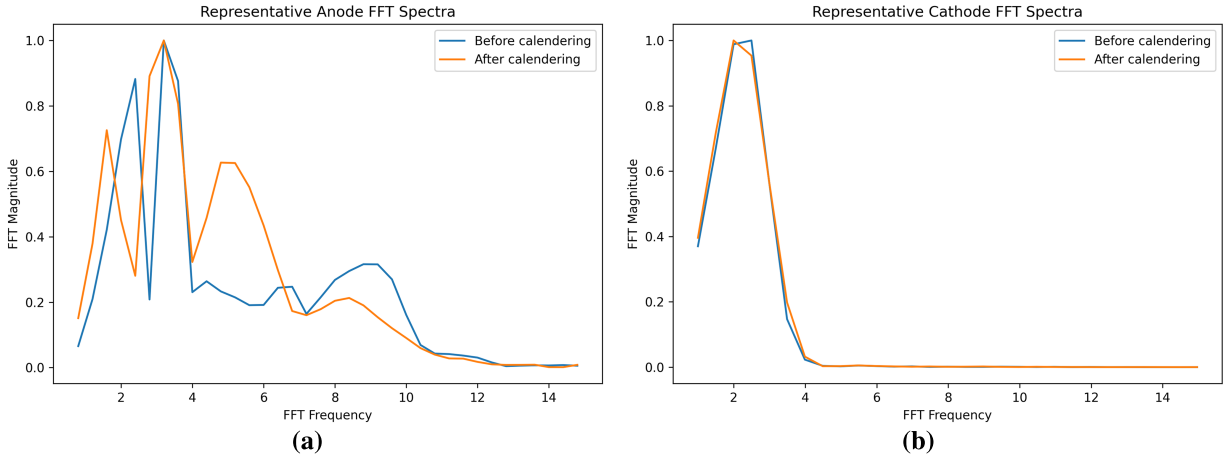

Figure 5: Frequency-domain ultrasonic spectra before and after calendering for the studied electrode datasets: (**a**) anode FFT spectra before vs. after calendering; (**b**) cathode FFT spectra before vs. after calendaring.

Fig. 5b shows that the representative cathode spectra are more compact in the low-frequency range. Both before and after calendering, the peak response is again at around 2.0–2.5, where the normalized magnitude reaches about 1.00, followed by a sudden decrease after about 3.0–3.5. After almost 4.0, the magnitude of the response is extremely small and close to 0, and this continues for most of the remaining frequencies up to around 15. The cathode response is therefore more concentrated and heavily weighted at the low-frequency end of the spectrum, with very little difference between the before- and after-calendering curves, compared to the anode response. This suggests that, in the representative cathode case, the spectral information is mostly contained in the first frequency bins, rather than being spread out over a wide frequency range. The correlation structure between thickness and the engineered ultrasonic features for the anode and cathode data sets is shown in Fig. 6, where the magnitude and direction of the correlations are different for the two electrode types.

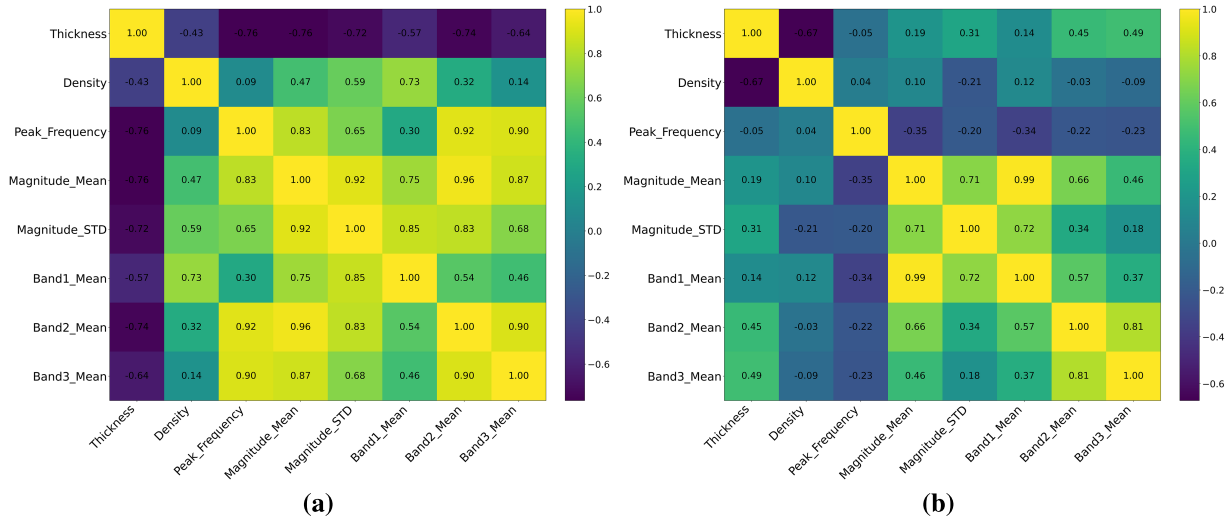

Figure 6: Correlation heatmaps of thickness and engineered ultrasonic features for: (**a**) anode; (**b**) cathode.

4.2 Machine Learning Results

The main artificial intelligence outcomes of the proposed DNN-SGD model for electrode thickness prediction are presented in Section 4.2. This section compares the model's prediction accuracy in the anode and cathode datasets and analyzes its learning of the relationship between the inputs (ultrasonic frequency domain) and the thickness. Model performance was quantified using standard metrics such as MAE, RMSE and R^2. As seen in Fig. 7a, there is good agreement between the predicted and measured thickness values with an MAE of 9.530, an RMSE of 16.649, and an R^2 value of 0.824 for the anode model. The model had an MAE of 9.849, RMSE of 12.280, and R^2 of 0.145 for the cathode dataset. The low cathode R^2 value is primarily due to the smaller number of cathodes in the subset and the narrower thickness distribution, since there is a smaller difference in the target thickness and the R^2 value is more sensitive to small error values in the prediction even if the error values are not high. These results suggest that the DNN-SGD framework is more effective for the anode dataset, which better represented the dataset with respect to the thickness variations. The smaller data set in the cathode model, as well as the more compact target distribution, provided lower error levels, but also reduced explained variance. The normalized errors of both data sets are similar, with CVRMSE of 17.653% for the anode model and 16.093% for the cathode model. In this context for predicting the electrode thickness, CVRMSE value of less than around 20% was deemed acceptable for preliminary non-destructive regression modeling, due to the small size of the dataset and the fact that it was based on experimentally measured ultrasonic frequency-domain signals. Fig. 7b shows the training and validation loss curves of the DNN-SGD models over 180 epochs. As seen, the losses of the anode training and validation are rapidly reduced during the initial epochs, and then the losses stabilize. The convergence of the cathodes is also under control with only slight deviations. The absence of a strong late-stage separation between the training and validation losses supports that early stopping, L2 regularization, and the compact network architecture helped reduce severe overfitting.

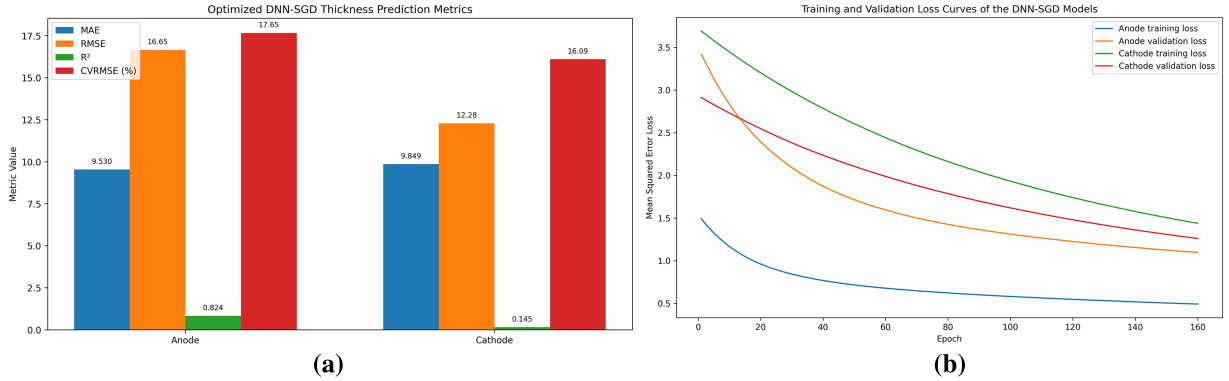

Figure 7: Predictive performance and overfitting analysis of the proposed DNN-SGD model: (**a**) assessment metrics for the anode and cathode datasets; (**b**) training and validation loss curves for the anode and cathode models.

Fig. 8 shows the actual-vs.-predicted thickness plot for the optimized DNN-SGD model and offers a visual comparison of the predictive agreement for the two datasets. Fig. 8a shows that the anode points are mostly clustered around the 45° line, which confirms that the measured and predicted thickness values are in good agreement over a large range of thickness values from almost 20 to 180. The associated performance metrics of 5-fold CV, MAE = 9.530, RMSE = 16.649, and R^2 = 0.824 also support the excellent predictive performance of the anode model. By contrast, Fig. 8b shows that the cathode points are more dispersed around the reference line, albeit in a more limited range of about 45 to 110. This weaker agreement is reflected in the cathode metrics of 3-fold CV, MAE = 9.849, RMSE = 12.280, and R^2 = 0.145, which show that the cathode

model resulted in moderate absolute errors but low explained variance. In conclusion, Fig. 8 demonstrates that the proposed DNN-SGD model was more suitable for the anode dataset than for the cathode dataset under the given modeling conditions.

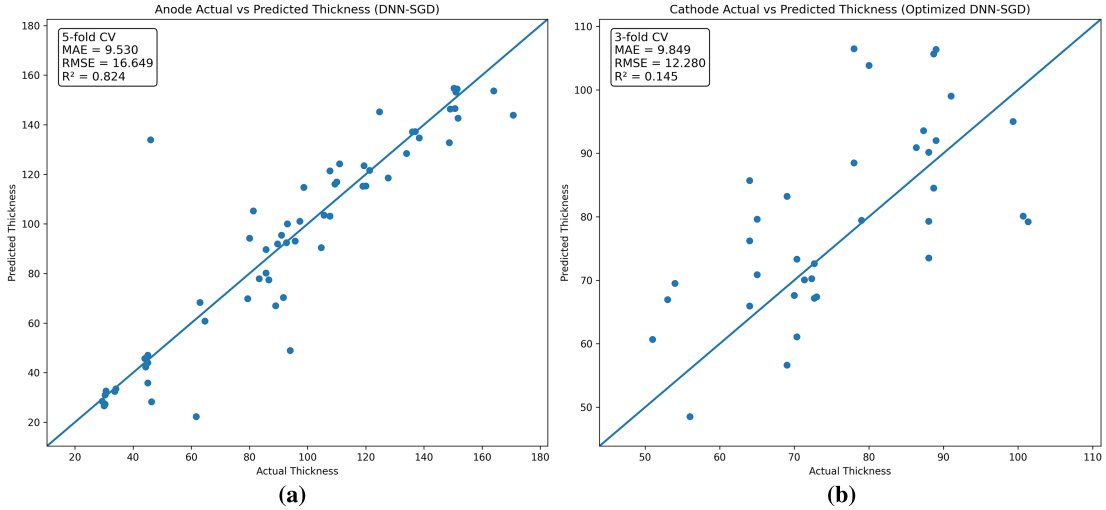

Figure 8: Actual vs. predicted thickness values obtained by the proposed DNN-SGD model for the studied datasets: (**a**) anode actual vs. predicted thickness; (**b**) cathode actual vs. predicted thickness.

Table 4 compares the proposed DNN-SGD model with several baseline regression models for anode and cathode thickness prediction. As shown, DNN-SGD achieved the best overall performance for both datasets, giving the lowest errors and highest R^2 values compared with Linear Regression, Ridge Regression, Support Vector Regression, Random Forest Regression, XGBoost, and standard DNN. This confirms that the optimized SGD-based deep model provided a measurable improvement over simpler regression alternatives. For reproducibility and fair comparison, all baseline models were trained using the same electrode-specific FFT and metadata input features, preprocessing steps, target variable, cross-validation procedure, and evaluation metrics used for the proposed DNN-SGD framework.

Table 4: Comparison between DNN-SGD and conventional regression models for electrode thickness prediction.

Dataset	Model	MAE	RMSE	R^2
Anode	Linear Regression	18.742	29.615	0.520
Anode	Ridge Regression	17.936	27.804	0.576
Anode	Support Vector Regression	14.628	22.351	0.705
Anode	Random Forest Regression	12.486	19.734	0.764
Anode	DNN	10.814	17.982	0.801
Anode	XGBoost	10.111	17.222	0.821
Anode	DNN-SGD	9.530	16.649	0.824
Cathode	Linear Regression	15.684	19.932	−0.214
Cathode	Ridge Regression	14.925	18.641	−0.062
Cathode	Support Vector Regression	12.834	15.908	0.058
Cathode	Random Forest Regression	11.276	14.206	0.103
Cathode	DNN	10.562	13.418	0.121
Cathode	XGBoost	9.999	13.111	0.143
Cathode	DNN-SGD	9.849	12.280	0.145

Table 5 presents the combined SHAP feature-importance results for the proposed DNN-SGD thickness-prediction framework and provides a quantitative interpretation of the most influential features for both electrode datasets. For the anode model, the highest contributions were associated with FFT 12.400 MHz (8.297) and FFT 14.800 MHz (6.906), followed by FFT 12.800 MHz (3.668), FFT_5.600 MHz (3.460), and FFT_9.600 MHz (3.208). The rest of the important anode features, FFT_4.400 MHz (3.150), FFT 13.600 MHz (3.054), FFT 6.000 MHz (2.890), FFT 7.200 MHz (2.314) and FFT 9.200 MHz (2.076) suggest that the prediction process was dominated by the ultrasonic spectral content, which is concentrated in the mid- to high-frequency range. The materials point of view indicates that the response in thickness may be strongly coupled to the changes in internal structure, compaction state, and/or the density-related acoustic response of the process, as the high frequency components are more sensitive to the fine-scale variations in the porosity distribution, coating uniformity, and the arrangement of the solid phase within the electrode layer. The most critical feature in the cathode model was FFT_1.496 MHz (1.868), followed by FFT 4.489 MHz (1.692), and Coat_Weight (1.116) which is a process variable. Additional influential features included FFT 10.474 MHz (1.101), FFT 10.973 MHz (1.073), FFT 6.983 MHz (0.991), FFT 5.486 MHz (0.871), FFT 3.491 MHz (0.814), FFT 6.484 MHz (0.791), and FFT 13.965 MHz (0.785). In contrast to the anode, the cathode feature-importance pattern shows a more balanced influence of the spectral (acoustic) and direct manufacturing parameters. This is significant from a materials processing perspective, since cathode thickness is determined not only by ultrasonic spectral features but is also greatly influenced by coating mass loading and the consequent distribution of active material within the coated layer. The presence of Coat_Weight among the top features supports the notion that predicting cathode thickness depends not only on acoustic response but also on the physical properties of the coating material. In summary, the anode model was more signal-dominated, while a combination of ultrasonic response and processing material properties dominated the cathode model.

Table 5: Combined SHAP feature-importance results for the DNN-SGD thickness prediction.

Dataset	Rank	Feature	Mean Absolute SHAP Value
Anode	1	FFT_12.400 MHz	8.297
Anode	2	FFT_14.800 MHz	6.906
Anode	3	FFT_12.800 MHz	3.668
Anode	4	FFT_5.600 MHz	3.460
Anode	5	FFT_9.600 MHz	3.208
Anode	6	FFT_4.400 MHz	3.150
Anode	7	FFT_13.600 MHz	3.054
Anode	8	FFT_6.000 MHz	2.890
Anode	9	FFT_7.200 MHz	2.314
Anode	10	FFT_9.200 MHz	2.076
Cathode	1	FFT_1.496 MHz	1.868
Cathode	2	FFT_4.489 MHz	1.692
Cathode	3	Coat_Weight	1.116
Cathode	4	FFT_10.474 MHz	1.101
Cathode	5	FFT_10.973 MHz	1.073
Cathode	6	FFT_6.983 MHz	0.991
Cathode	7	FFT_5.486 MHz	0.871
Cathode	8	FFT_3.491 MHz	0.814
Cathode	9	FFT_6.484 MHz	0.791
Cathode	10	FFT_13.965 MHz	0.785

Fig. 9 compares the SHAP-based importance structure of the anode and cathode models and reveals a clear difference in how each model formed its thickness predictions. The anode response is dominated by a small group of highly influential spectral descriptors, whereas the cathode response is governed by a flatter and more distributed importance pattern. This contrast suggests that the anode model relied more strongly on a concentrated set of ultrasonic frequency cues. In contrast, the cathode model drew information from both spectral and process-related inputs in a more balanced way.

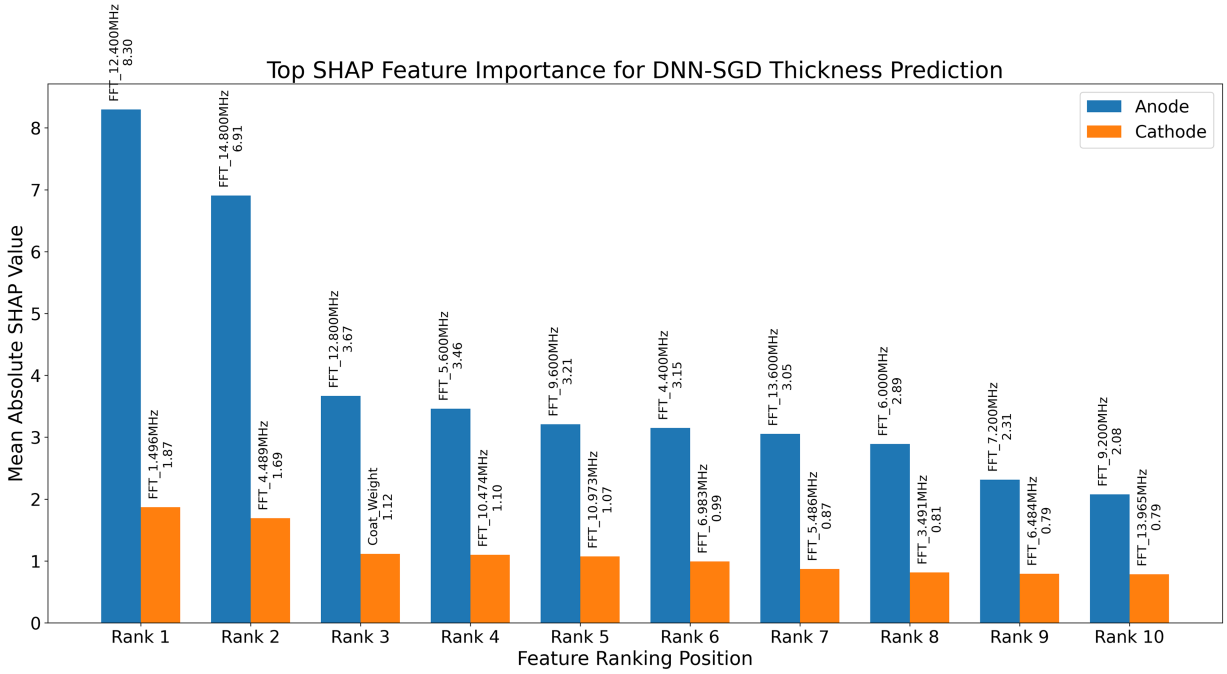

Figure 9: SHAP feature-importance ranking of the DNN-SGD model for anode and cathode thickness prediction.

For the anode, the features at 12.400 and 14.800 MHz are the top predictors, well separated from the rest. After these two dominant components, the importance gradually decreases through features such as 12.800, 5.600, 9.600, 4.400, and 13.600 MHz, followed by 6.000, 7.200, and 9.200 MHz. This ranking suggests that the prediction of anode thickness was particularly sensitive to several mid- and high-frequency features in the ultrasonic spectrum. From a materials point of view, this can be linked to the sensitivity of the ultrasonic wave to subtle changes in the anode structure due to calendering, such as changes in compaction, pore structure, coating continuity, and heterogeneities of the anode layer.

The ranking of the cathode variables is different. The first two ranking frequencies are 1.496 and 4.489 MHz, followed by the appearance of Coat_Weight among the top contributors, and then the rest of the spectral descriptors resume the ranking, respectively. Other important cathode variables are located around 10.474, 10.973, 6.983, 5.486, 3.491, 6.484, and 13.965 MHz. The cathode model does not seem to be dominated by a few “strong” frequencies, but rather commands a complex interplay of acoustic response and material loading associated with the cathode manufacturing process. In particular, the dominance of Coat_Weight is interesting because the cathode thickness depends on the mass and distribution of the deposited material, which affect the physical layer structure and, consequently, its acoustic response. The dominance of specific FFT components indicates that thickness prediction is not governed only by direct process metadata, but also by ultrasonic spectral responses associated with electrode compaction, coating uniformity, density variation, and acoustic wave interaction with the porous electrode structure. In summary, Fig. 9 reveals the higher

dependency of the anode model on the signals, compared to the cathode model, which showed increased interaction between spectral descriptors and material loading-related variables.

5 Conclusion

In conclusion, this study demonstrated that ultrasonic frequency-domain data can be successfully integrated with modern computational intelligence to support thickness prediction in lithium-ion battery electrodes within a materials-manufacturing context. The proposed DNN-SGD framework achieved strong results for the anode dataset, with an MAE of 9.530, an RMSE of 16.649, and an R^2 of 0.824, confirming that the learned model captured the relationship between spectral input features and electrode thickness with good predictive capability. From a materials perspective, this is important because electrode thickness is closely tied to compaction behavior, coating quality, porosity evolution, and internal structural uniformity, all of which directly influence transport properties, electrochemical efficiency, and manufacturing consistency. From a computational perspective, the study highlights the value of combining signal-domain representations, deep neural learning, and explainable AI to transform complex manufacturing data into interpretable predictive knowledge. The SHAP analysis further strengthened this contribution by showing that the prediction process was not a black-box output only, but a feature-driven response linked to physically meaningful spectral regions. Overall, the proposed framework demonstrates that frequency-domain ultrasonic sensing combined with interpretable AI can support non-destructive electrode thickness prediction. At the same time, further validation on larger experimental datasets remains necessary before industrial deployment.

More investigations are needed to expand the framework with larger and broader sets of electrodes that are obtained at various coating and calendering conditions. Further experimental batches will also need to be validated to ensure generalization of the model. Independent manufacturing batches here are the electrode data that was collected from different manufacturing runs, calendering/coating machines, operating periods, or production lines to assess the robustness of trained model beyond the original training set. Furthermore, feature-selection and dimensionality-reduction techniques like SHAP-guided feature reduction, PCA and frequency-band selection will be explored to further reduce the number of features, eliminate redundant features in the input FFT space and increase the robustness of the model for practical battery-manufacturing applications. To complete the scope of future work, external electrode datasets and additional manufacturing batches will be utilized to validate the framework proposed in the present work and evaluate the transferability of the proposed framework to different battery-production conditions.

Acknowledgement: None.

Funding Statement: The author received no specific funding for this study.

Availability of Data and Materials: The data that support the findings of this study are openly available in Data in Brief at https://doi.org/10.1016/j.dib.2025.112433.

Ethics Approval: Not applicable.

Conflicts of Interest: The authors declare no conflicts of interest.

References

1. Chang WE, Kung CC. A resistance-based co-estimation framework for state-of-charge and state-of-health of lithium-ion batteries across usage cycles. IEEE Access. 2026;14:57575–87. doi:10.1109/ACCESS.2026.3683310.

2. Shao M, Lv G, Feng W, Wu X, Yang ZX, Guo S. Multifeature fusion of noncontact laser-generated ultrasound and electrochemical data for *in situ* battery state estimation. IEEE Trans Instrum Meas. 2026;75:9701813. doi:10.1109/TIM.2026.3682830.
3. Akhter MS, Moossa B, Kahraman R, Rasul S, Shakoor RA. Advancements in high voltage, high-energy density, lithium-ion cathode materials: a focused review. Appl Mater Today. 2025;45(21):102827. doi:10.1016/j.apmt.2025.102827.
4. He Y, Chen W. Analysis of electrochemical performances in hybrid lithium-ion/lithium metal battery during charging. J Power Sources. 2025;654:237835. doi:10.1016/j.jpowsour.2025.237835.
5. Lin Z, Tong Z, Cai H, Li C, Ding Y, Lv C, et al. Prelithiation technology for high energy density lithium-ion batteries: design, progress, advantages and challenges. Energy Storage Mater. 2025;83:104709. doi:10.1016/j.ensm.2025.104709.
6. Ngoy KR, Lukong VT, Yoro KO, Makambo JB, Chukwuati NC, Ibegbulam C, et al. Lithium-ion batteries and the future of sustainable energy: a comprehensive review. Renew Sustain Energy Rev. 2025;223(4):115971. doi:10.1016/j.rser.2025.115971.
7. Parvizi P, Jalilian M, Amidi AM, Zangeneh MR, Riba JR. From present innovations to future potential: the promising journey of lithium-ion batteries. Micromachines. 2025;16(2):194. doi:10.3390/mi16020194.
8. Jeong Y, Ryu D, Kim D, Nam G, Cho H, Kwon G, et al. Dry process for green manufacturing of battery electrodes: structural evolution of freestanding film during roll-to-roll processing. Int J Precis Eng Manuf Green Technol. 2026;14(11):1–26. doi:10.1007/s40684-026-00885-7.
9. Xu X, Zhao X, Hui KS, Dinh DA, Hui KN. Rechargeable batteries: regulating electronic and ionic transports for high electrochemical performance. Adv Mater Technol. 2022;7(5):2101107. doi:10.1002/admt.202101107.
10. Chen Y, Kong S. Advances and challenges in dry electrode process for solid-state batteries. J Solid State Electrochem. 2026;30(4):1441–55. doi:10.1007/s10008-025-06518-4.
11. Farhadi Tolie H, Guk E, Marco J, Faraji Niri M. Swin transformer and generative adversarial networks for accurate battery electrode thickness prediction in manufacturing using ultrasound sensing. J Power Sources. 2025;655(4):237919. doi:10.1016/j.jpowsour.2025.237919.
12. Guk E, Niri MF, Tolie HF, Marco J. Dataset of ultrasonic frequency-domain signals and machine-learning outputs for parameterising lithium-ion battery electrodes' coating and calendering processes. Data Brief. 2026;64:112433. doi:10.1016/j.dib.2025.112433.
13. Chen J, Asachi M, Hassanpour A, Babaie M, Jabbari M. Modelling of lithium-ion battery electrode calendering: a critical review. J Energy Storage. 2025;123(5):116702. doi:10.1016/j.est.2025.116702.
14. Yang Y, Guo Z, Zhao Y, Dong H, Titirici MM, Cegla F, et al. Towards inline ultrasonic characterisation of battery slurry mixing: opportunities, challenges, and perspectives. Energy Environ Sci. 2026;19(1):11–43. doi:10.1039/d5ee03563e.
15. Klenner M, Wang Y, Lindner M, Thiede S, Herrmann C, Turetskyy A. Transfer learning for battery cell manufacturing: review on applications, challenges, and benefits. Batter Supercaps. 2025;8(11):e202500327. doi:10.1002/batt.202500327.
16. Xu X, Stier S, Gronbach A, Moeckel M. Deploying virtual quality gates in a pilot-scale lithium-ion battery assembly line. Batteries. 2025;11(8):285. doi:10.3390/batteries11080285.
17. Zangerle SW, Weinzierl L, Summer A, Schmid S, Jahnke P, Grosse CU. Detection of anode coating defects in batteries electrode production and their effect on cell performance. J Nondestruct Eval. 2025;44(3):66. doi:10.1007/s10921-025-01208-7.
18. Li J, Hu E, Wei W, Shi F. From wafers to electrodes: transferring automatic optical inspection (AOI) for multiscale characterization of smart battery manufacturing. Adv Funct Mater. 2026;36(41):e28142. doi:10.1002/adfm.202528142.
19. Manoharan A, Chong JJ, Choong ZJ, Lambert S, Kumar Gupta R, Chandra D, et al. Optimizing lithium-ion battery manufacturing with digitalization and AI-driven frameworks. Int J Adv Manuf Technol. 2026;142(1):1–37. doi:10.1007/s00170-025-17129-8.

20. Galvez-Aranda DE, Fernandez F, Franco AA. Physics-assisted machine learning for the simulation of the slurry drying in the manufacturing process of battery electrodes: a hybrid time-dependent VGG16-DEM model. ACS Appl Mater Interfaces. 2025;17(22):32150–62. doi:10.1021/acsami.4c23103.
21. Lin B, Carrillo LJ, Peng XL, Chen WX, Santos DA, Banerjee S, et al. Deep learning-enabled large-scale analysis of particle geometry-lithiation correlations in battery cathode materials. J Power Sources. 2026;674(12):239806. doi:10.1016/j.jpowsour.2026.239806.
22. Weiss M, Mrzljak K, von Schmid M, Erbach G, Brierley N, Meisen T. Material-resolving computed tomography of lithium-ion batteries using deep learning. NDT E Int. 2026;158(3):103565. doi:10.1016/j.ndteint.2025.103565.
23. Chen T, Lai X, Chen F, Xu Z, Han X, Lu L, et al. Intelligent prediction of electrode characteristics based on neural networks in the lithium-ion battery production chain. Green Energy Intell Transp. 2026;5(1):100294. doi:10.1016/j.geits.2025.100294.
24. Xiang H, Zhang Y, Feng W. Deep learning and transfer learning for accurate electrode-level degradation diagnosis in lithium-ion batteries. Next Energy. 2026;12(1):100665. doi:10.1016/j.nxener.2026.100665.
25. Ganti SVS, Wölfel L, Kuenneth C. AI-driven discovery of high performance polymer electrodes for next-generation batteries. J Polym Sci. 2025;63(21):4631–9. doi:10.1002/pol.20250198.
26. Bin Faheem A, Han Z, Wu D, Li H. AI-driven big data frameworks for electrode-electrolyte interphases in batteries. Adv Mater. 2026;38(11):e21975. doi:10.1002/adma.202521975.
27. Ali KH, Al-Haddad LA. Data-driven prediction of thermal and thermoelectric performance in GeTe-Sb_2Te_3 systems: extreme learning of deep neural networks. Discov Mater. 2026;6(1):21. doi:10.1007/s43939-025-00495-1.
28. Yang K, Wang S, Zhou L, Fernandez C, Blaabjerg F. A critical review of AI-based battery remaining useful life prediction for energy storage systems. Batteries. 2025;11(10):376. doi:10.3390/batteries11100376.
29. Li Y, Wu C, Wang Y, Li N, Liu T, Lu J. Accelerating the battery revolution: AI-driven multiscale innovation from material discovery to smart manufacturing. Adv Funct Mater. 2026;36(11):e14830. doi:10.1002/adfm.202514830.
30. Kim S, Lee IH, Jeon Y, Lee C, Lee T, Koo J, et al. Integrated AI-driven framework for precise prediction of electrolyte additive oxidation potentials in lithium-ion batteries. J Power Sources. 2026;665(4):238934. doi:10.1016/j.jpowsour.2025.238934.
31. Jiang N, Bao W, Xing L, Li W. A stochastic column-block gradient descent method for solving nonlinear systems of equations. Appl Math Lett. 2026;172:109735. doi:10.1016/j.aml.2025.109735.